ACS NANO
Cite This: ACS Nano XXXX, XXX, XXX–XXX
www.acsnano.org

ARTICLE

# Iodine Vapor Transport-Triggered Preferential Growth of Chevrel $Mo_6S_8$ Nanosheets for Advanced Multivalent Batteries

Minglei Mao,[†,∥] Zejing Lin,[†,∥] Yuxin Tong,[†] Jinming Yue,[†] Chenglong Zhao,[†] Jiaze Lu,[†] Qinghua Zhang,[†] Lin Gu,[†] Liumin Suo,[*,†,‡,§] Yong-Sheng Hu,[†] Hong Li,[†] Xuejie Huang,[†] and Liquan Chen[†]

[†]Key Laboratory for Renewable Energy, Beijing Key Laboratory for New Energy Materials and Devices, Institute of Physics, Chinese Academy of Sciences, Beijing 100190, China

[‡]Center of Materials Science and Optoelectronics Engineering, University of Chinese Academy of Sciences, Beijing 100049, China

[§]Yangtze River Delta Physics Research Center Co. Ltd., Liyang, Jiangsu 213300, China

Supporting Information

**ABSTRACT:** **Owing to its unique structure, Chevrel phase (CP) is a promising candidate for applications in rechargeable multivalent (Mg and Al) batteries. However, its wide applications are severely limited by time-consuming and complex synthesis processes, accompanied by uncontrollable growth and large particle sizes, which will magnify the charge trapping effect and lower the electrochemical performance. Here, an iodine vapor transport reaction (IVT) is proposed to obtain large-scale and highly pure $Mo_6S_8$ nanosheets, in which iodine helps to regulate the growth kinetics and induce the preferential growth of $Mo_6S_8$, as a typical three-dimensional material, to form nanosheets. When applied in rechargeable multivalent (Mg and Al) batteries, $Mo_6S_8$ nanosheets show very fast kinetics owing to the short diffusion distance, thereby exhibiting lower polarization, higher capacities, and better low-temperature performance (up to −40 °C) compared to that of microparticles obtained *via* the conventional method. It is anticipated that $Mo_6S_8$ nanosheets would boost the application of Chevrel phase, especially in areas of energy storage and catalysis, and the IVT reaction would be generalized to a wide range of inorganic compound nanosheets.**

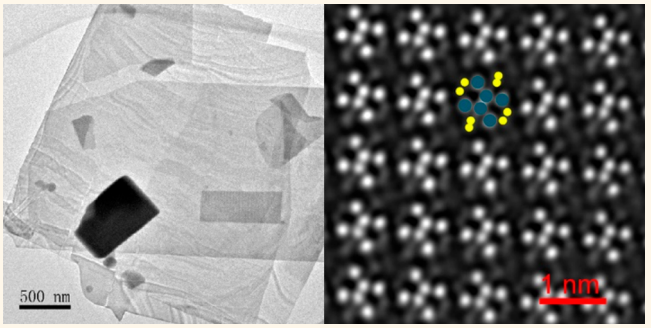


**KEYWORDS:** *Chevrel phase nanosheets, iodine vapor transports, preferential growth, rechargeable Mg and Al batteries, fast kinetics*

Chevrel phase (CP) compounds are molybdenum chalcogenides composed of $Mo_6T_8$ or $M_xMo_6T_8$ (M = metal, T = S, Se, or Te), which were discovered by Chevrel *et al.* in 1969.[1,2] Chevrel phase has a unique structure, with six Mo atoms located on the faces of a slightly distorted cube forming an octahedron cluster ($Mo_6$) and eight T anions ($T_8$) occupying the corners of the cube.[3,4] Between closely packed clusters, there are relatively large open spaces with three-dimensional (3D) channels.[5,6] Owing to the unique structure, Chevrel phase, over the past five decades, has been applied in superconductivity,[7,8] thermoelectricity,[9,10] catalysis,[11,12] and electrodes for secondary batteries.[13,14] Since CP $Mo_6S_8$ was first employed in the prototype of rechargeable Mg batteries in 2000,[13] its scope of application has been largely extended to almost all secondary batteries. Various metal ions, including monovalent cations ($Li^+$,[15,16] $Na^+$,[17−19] and $Cu^+$),[20] divalent cations ($Mg^{2+}$,[21,22] $Zn^{2+}$,[19,23] $Ni^{2+}$,[24] $Mn^{2+}$,[24] $Cd^{2+}$,[19] and $Co^{2+}$), and trivalent cations ($Al^{3+}$),[25] have been reported to intercalate CPs. Until now, CPs are still the most successful cathodes for rechargeable multivalent batteries.[26] However, due to the sluggish kinetics of microsized bulk $Mo_6S_8$, it is hard to avoid the charge trapping effect of insertion ions (especially multivalent ions), resulting in low Coulombic efficiency and gradual capacity decay. In order to improve the kinetics of $Mo_6S_8$, the nanosizing strategy is adopted to reduce diffusion distance of intercalated ion.[27]

However, it is still challenging to approach large-scale and high-quality nanosized $Mo_6S_8$. Currently, all available methods including a solid-state method,[16,28−36] a molten salt route (MS),[37] a self-propagating high-temperature synthesis (SHS),[38] a high-energy mechanical milling (HEMM),[39] and

Received: November 8, 2019
Accepted: December 30, 2019
Published: December 30, 2019






DOI: 10.1021/acsnano.9b08848
ACS Nano XXXX, XXX, XXX–XXX

**Scheme 1. Schematic Illustration of the Iodine Vapor Transport Method for $Mo_6S_8$ Nanosheets**

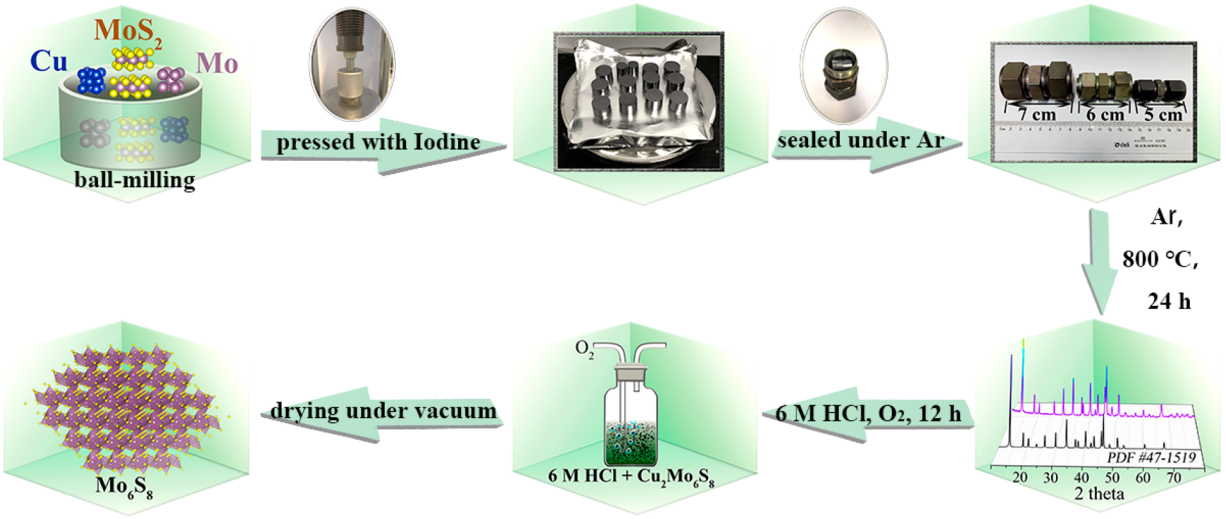


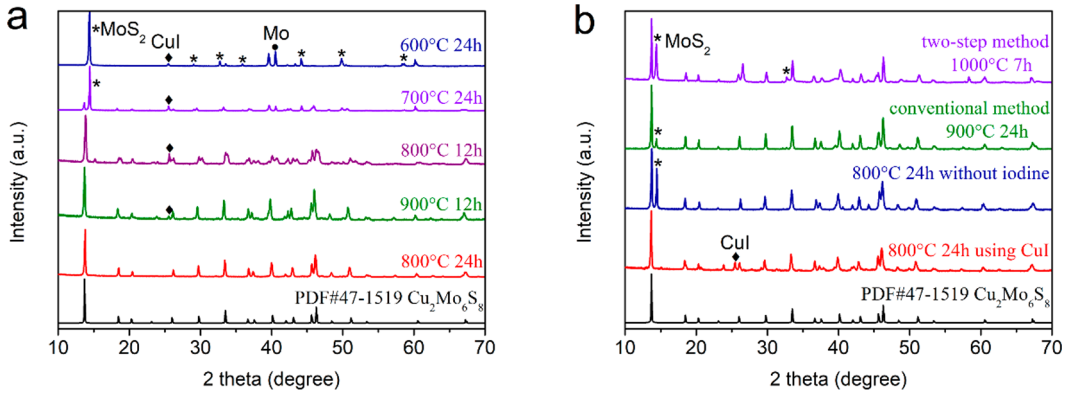


**Figure 1. (a) XRD patterns of $Cu_2Mo_6S_8$ samples prepared at various temperatures (from 600 to 900 °C) and reaction times (12 or 24 h). (b) XRD patterns of $Cu_2Mo_6S_8$ synthesized by the two-step method, conventional method, and our method without iodine or using CuI.**

a two-step solution chemistry route[21,27] suffer from either high energy consumption, impurities, or uncontrollable particle growth. Traditionally, the solid-state method requires pretty high temperatures (1100−1200 °C) with Cu, Mo, and S mixtures sealed in an evacuated quartz ampule (EQA) for 7 days.[36] The process is time-consuming and dangerous due to the high vapor pressure of sulfur inside the EQA at high temperature. To avoid the potential safety issue, metal sulfides (CuS, $MoS_2$) are employed as the sulfur source, sealed in an argon-sealed Swagelok vessel instead of EQA. However, the reaction temperature is still more than 900 °C, which also produces microsized CP with some unavoidable impurity ($MoS_2$), as the decomposition of CuS at 220 °C produces sulfur vapor and escapes during heating. Although the two-step solution chemistry route enables $Mo_6S_8$ nanocubes,[21,27] the synthesis process is cumbersome and error-prone, and hydrogen flow serves as a reducing agent throughout the reaction. Recently, halogens such as $I_2$ and $Br_2$,[40] as well as alkali metal halides,[41,42] have been reported to tune the growth kinetics and facilitate the formation of two-dimensional (2D) transition-metal chalcogenide (TMC) nanosheets. Halogen molecules or halides are employed as reaction promoters to lower the melting points of reactants, facilitate the formation of intermediate products, and increase the overall growth rate of TMC nanosheets. Inspired by the success of halogens in 2D TMCs, we attempt to introduce the halogen as the manipulator of preferential flat growth to form the nanosheet $Mo_6S_8$, which possess a large surface area, high aspect ratio, and unusual surface chemistry and hence immense potential for application in batteries.

In this work, the iodine vapor transport reaction (IVT) is proposed to synthesize large-scale and high-purity $Mo_6S_8$ nanosheets, in which iodine serves to modulate the growth kinetics and induce the preferential flat growth of $Mo_6S_8$ to form nanosheets. Nanosheets are obtained in the typical 3D material of $Mo_6S_8$. Meanwhile, IVT accelerates the solid-state reaction with the lower reaction temperature and the shorter duration. Compared with the microsized $Mo_6S_8$, our $Mo_6S_8$ nanosheet cathodes show excellent electrochemical performance in both rechargeable Mg and Al batteries, whose advantage is far more obvious at low temperatures.

## RESULTS AND DISCUSSION

In a typical synthesis process of $Cu_2Mo_6S_8$, $MoS_2$, Cu, and Mo powders in a molar ratio of 2:1:1 were ball-milled under Ar (Scheme 1). Then, the mixtures along with a small amount of iodine were pressed into pellets and sealed in a Swagelok stainless steel vessel, which was gradually heated to 800 °C at 2 °C/min and kept for 24 h in an argon atmosphere. To investigate the optimal reaction conditions, the reaction was carried out in a wide range of temperatures (from 600 to 900 °C) and durations (12 or 24 h) (Figure 1a). The main X-ray


DOI: 10.1021/acsnano.9b08848
ACS Nano XXXX, XXX, XXX−XXX

diffraction (XRD) peaks at 600 °C for 24 h are indexed to $MoS_2$ with a small peak for CuI, indicating that Cu and iodine only react to form CuI, and the temperature of 600 °C is not high enough for the formation of $Cu_2Mo_6S_8$. Upon increasing the temperature to 700 °C, a small peak corresponding to $Cu_2Mo_6S_8$ (13.7°) appears along with weakening Mo peaks, but the main peak at 14.4° still belongs to $MoS_2$. At 800 °C, most peaks can be indexed to $Cu_2Mo_6S_8$ after 12 h with slight amounts of CuI and Mo remaining, whereas highly pure $Cu_2Mo_6S_8$ is obtained after 24 h, in which all the peaks of $Cu_2Mo_6S_8$ can be well indexed to standard PDF#47-1519.[43,44] When further elevating the temperature up to 900 °C, we found that a little CuI remains in final products after 12 h, revealing that exorbitant temperature is not beneficial for pure $Cu_2Mo_6S_8$. Therefore, a temperature of 800 °C for 24 h is optimal for highly pure $Cu_2Mo_6S_8$.

To investigate the effect of iodine on the $Cu_2Mo_6S_8$ formation, the preparation process and conditions are fixed with the only variation of iodine (Figure 1b). $Cu_2Mo_6S_8$ is obtained with some $MoS_2$ remaining, demonstrating that iodine is indispensable for pure $Cu_2Mo_6S_8$. To further investigate the reaction path, CuI instead of Cu and $I_2$ is used as a raw material along with $MoS_2$ and Mo powders (1:2:1 in molar ratio), in which pure $Cu_2Mo_6S_8$ is obtained with few CuI left. The reaction mechanism is illustrated below (Scheme 2). Iodine will first sublimate to be iodine vapor (eq 1) and react with Cu, generating solid CuI (eq 2), which liquefies at ~600 °C (eq 3). Finally, CuI(l) reacts with Mo(s) and $MoS_2$(s) to produce $Cu_2Mo_6S_8$ and releases iodine at 800 °C (eq 4).

**Scheme 2. Schematic Illustration of Reaction Path To Synthesize $Cu_2Mo_6S_8$, in Which Iodine Is Recyclable**

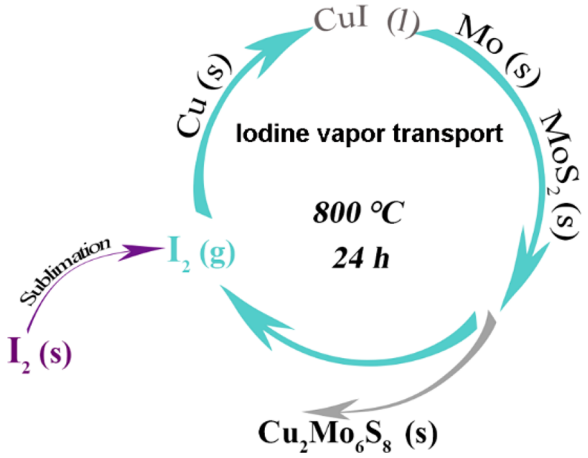


$$I_2(s) \xrightarrow{\text{sublimation}} I_2(g) \quad (1)$$

$$2Cu(s) + I_2(g) \rightarrow 2CuI(s) \quad (2)$$

$$CuI(s) \xrightarrow{600\ ^\circ C} CuI(l) \quad (3)$$

$$4MoS_2(s) + 2CuI(l) + 2Mo(s) \xrightarrow{800\ ^\circ C} Cu_2Mo_6S_8(s) + I_2(g) \quad (4)$$

To highlight the IVT reaction, the two-step method[27] and conventional method[36,45] were also performed for synthesizing $Cu_2Mo_6S_8$ (Figure 1b). Both methods generate $Cu_2Mo_6S_8$ with some impure $MoS_2$. The two-step method including solution processing and solid-state reaction is tedious in steps, which readily introduces impurities and might cause safety issues because of the mandatory use of hydrogen gas during the sulfurization and final reduction of the sulfur compounds at high temperatures (1000 °C).[27] The conventional method is most widely used to synthesize $Cu_2Mo_6S_8$, in which CuS, $MoS_2$, and Mo are sealed in a Swagelok vessel and kept at 900 °C for 24 h.[36] However, CuS will decompose at ~220 °C into sulfur vapor, which might escape from the Swagelok vessel (which is not so tight as the quartz ampule), producing some nonstoichiometric impurities (Figure 1b).

Pure $Mo_6S_8$ was obtained by leaching out Cu from an as-prepared $Cu_2Mo_6S_8$ precursor (Figure S1) in a 6 M HCl solution for 12 h with oxygen bubbling.[45,47] The XRD patterns of $Mo_6S_8$ well match the standard PDF#89-5114,[45] which exhibits a rhombohedral structure with the $R\bar{3}$ space group (Figure 2a). $Mo_6S_8$ nanosheets with various sizes are revealed by scanning electron microscopy (SEM) (Figure S2) and transmission electron microscopy (TEM) (Figure 2b,c), in which the lateral length reaches several micrometers with the thickness of tens of nanometers. $Mo_6S_8$ nanosheets are single-crystalline with a (101) rhombohedral lattice spacing of 6.43 Å,[27,39] revealed by high-resolution transmission electron microscopy (HRTEM) and corresponding fast Fourier transform (FFT) (Figure 2d). To further confirm the Chevrel phase of $Mo_6S_8$ nanosheets, spherical aberration-corrected scanning transmission electron microscopy (STEM) is employed to obtain a direct vision of the atomic structure (Figure 2e). Each atomic column in the low-angle annular dark-field (LAADF) image can be directly associated with their chemical identities using the image contrast. Accordingly, six molybdenum atoms and eight sulfur atoms can be clearly observed in the [211] direction,[23,48,49] confirmed by the representative line intensity profile in Figure 2f.

The electrochemical performance of $Mo_6S_8$ nanosheets in both rechargeable Mg batteries (RMBs) and rechargeable Al batteries (RABs) was evaluated (Figure 3 and Figures S8–S15). In RMBs, the nanosheet $Mo_6S_8$ cathode delivers high initial discharge and charge capacities of 123 and 115 mA h/g at 0.1C (1C = 128 mA/g) (Figure S8), corresponding to a Coulombic efficiency (CE) of 93.4%, much higher than 73.5% of $Mo_6S_8$ microparticles, revealing that $Mo_6S_8$ nanosheets effectively reduce the intercalated $Mg^{2+}$ trapped.[50] A lower overpotential of $Mo_6S_8$ nanosheets indicates faster Mg intercalation kinetics (Figure S8), which is also evidenced by cyclic voltammetry (Figure 3a). In the second and third cycles for RMBs, two discharge plateaus at 1.2 and 1.1 V (Figure S12) correspond to two different Mg insertion sites named inner and outer rings.[4,51] The minimal distance between the inner sites (0.9 Å) is twice shorter than that between the inner and outer sites (2.0 Å), causing a higher possibility of $Mg^{2+}$ hopping between the inner sites than between inner and outer sites.[4] As a result, $Mg^{2+}$ undergoes a circuit motion, instead of progressive diffusion in the bulk of $Mo_6S_8$, accounting for an essential amount of $Mg^{2+}$ trapped in the $Mo_6S_8$ host.

The rate capability of the nanosheet $Mo_6S_8$ cathodes is further evaluated for both RMBs and RABs (Figure 3b,c and d,e). Compared with microsized $Mo_6S_8$ (Figures S14 and S15), $Mo_6S_8$ nanosheets show lower overpotentials (Figure 3b,d) and higher capacities (Figure 3c,e) in the entire range of the examined current densities. To further investigate the


DOI: 10.1021/acsnano.9b08848
ACS Nano XXXX, XXX, XXX−XXX

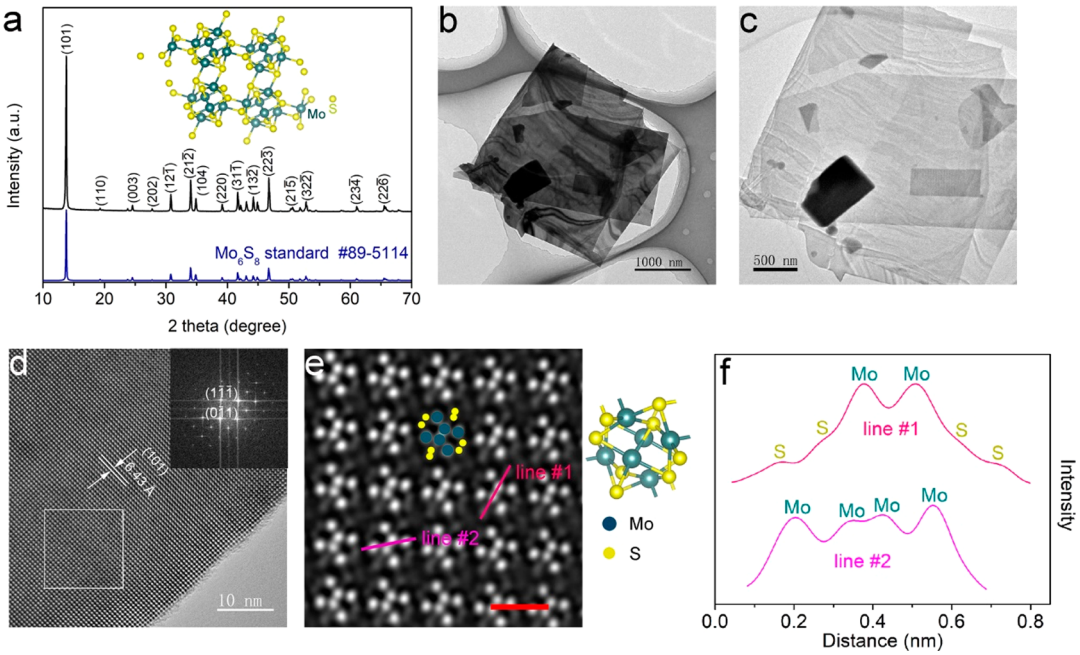


**Figure 2. (a) XRD patterns of $Mo_6S_8$ nanosheets with standard PDF#89-5114. Inset shows the crystal structure of $Mo_6S_8$, in which yellow and cyan balls represent sulfur and molybdenum atoms, respectively. Image prepared with VESTA.[46] (b,c) TEM images of $Mo_6S_8$ nanosheets. (d) HRTEM image of the lattice structure of a $Mo_6S_8$ crystal aligned on a zone axis where the rhombohedral lattice spacing can be resolved. Inset shows the FFT. (e) STEM-LAADF image of the single crystal of $Mo_6S_8$ along the [211] zone axis. The bright and gray spots correspond to molybdenum and sulfur atoms, respectively. Scale bar, 1 nm. (f) Line intensity profiles along the highlighted pink and magenta lines in (e). Four sulfur and two molybdenum atoms in line #1 and four molybdenum atoms in line #2.**

kinetics,[52] galvanostatic intermittent titration technique (GITT) is applied to capture quasi-equilibrium states with 1 h relaxation at open circuit to reach quasi-equilibrium after each 0.5 h discharging or charging at 10 mA/g (Figure 3f). Apparently, the overpotentials of $Mo_6S_8$ nanosheets are lower than those of microparticles, confirming the faster intercalation kinetics. The long-term cycling stability of $Mo_6S_8$ is evaluated at room temperature (Figure 3g,h). After 500 cycles in RMBs, $Mo_6S_8$ nanosheets retain a capacity of 89 mA h/g, as compared to 70.3 mA h/g of $Mo_6S_8$ microparticles (Figure 3g). In RABs, $Mo_6S_8$ nanosheets deliver a capacity of 68 mA h/g after 200 cycles, higher than 45 mA h/g of microparticles (Figure 3h).

To further investigate the fast kinetics of $Mo_6S_8$ nanosheets, low-temperature electrochemical performance in RMBs and RABs is examined (Figure 4 and Figures S18–S22). In the whole temperature range of −40 to 20 °C, $Mo_6S_8$ nanosheets release much higher capacities and lower overpotentials in both RMBs and RABs (Figure 4a,b,d,e and Figures S18 and S19). Even at the extremely low temperature of −40 °C, the nanosheet $Mo_6S_8$ cathode survives in RMBs,[53,54] delivering a capacity of ∼30 mA h/g, in contrast to the negligible capacity of $Mo_6S_8$ microparticles. When the temperature steps are repeated, the corresponding capacity recovers very well, indicating good temperature-abuse duration (Figure 4b,e). In the low-temperature cycle, $Mo_6S_8$ nanosheets are able to release much higher capacities after 50 cycles both in RMBs and RABs (Figure 4c,f). The low-temperature kinetics of $Mo_6S_8$ is also studied by GITT (Figure S21), in which the overpotentials climb gradually from 0 to −30 °C (Figure S22). The overpotentials of $Mo_6S_8$ nanosheets are always lower than those of microparticles, confirming the faster kinetics.

*Ex situ* XRD, energy-dispersive X-ray spectroscopy (EDS), and X-ray photoelectron spectroscopy (XPS) were conducted to investigate the intercalation mechanism of $Mg^{2+}$ into $Mo_6S_8$ nanosheets (Figures 5, 6, and S23). For the first discharge plateau (from point A to B), there is a phase transition from $Mo_6S_8$ ($R\bar{3}$) to $MgMo_6S_8$ ($P1$), followed by another phase transition to $Mg_2Mo_6S_8$ ($P\bar{1}$) in the second discharge plateau from B to D.[55] When recharged to point E and F, $MgMo_6S_8$ ($P1$) and $Mo_6S_8$ ($R\bar{3}$) recover, indicating the reversible phase transition. EDS mapping is also applied to study the magnesiation/demagnesiation process of $Mo_6S_8$ nanosheets, in which the amount of intercalated $Mg^{2+}$ for different discharged/charged states is consistent with corresponding specific capacity (Figure S23).

To understand the charge transfer mechanism of $Mo_6S_8$ upon galvanostatic magnesiation, *ex situ* XPS Mo 3d and S 2p are acquired (Figure 6), in which the C 1s peak at 284.8 eV is used as the reference binding energy (Figure S24). The Mo 3d peaks of pristine $Mo_6S_8$ are fitted with two asymmetric doublets—$Mo^{3+}$ and $Mo^{2+}$ in the sulfur environment. S 2p peaks can be fitted with two doublets: 4-coordinated $S^{2-}$ attributed to sulfur coordinated by four Mo atoms and 3-coordinated $S^{2-}$ attributed to sulfur coordinated by three Mo atoms.[6] Upon magnesiation from A to B (in the first discharge plateau), there is no evident evolution for two Mo 3d doublets, whereas the 3-coordinated $S^{2-}$ doublet disappears, accompanied by 4-coordinated $S^{2-}$ doublet being enhanced, indicating that only sulfur is reduced in this stage. During further insertion of $Mg^{2+}$ from B to D (the second discharge plateau), only the doublet of 4-coordinated $S^{2-}$ is evidenced and unchanged, whereas $Mo^{3+}$ gradually recedes and disappears until D (fully discharged) and $Mo^{2+}$ remains enhanced. During demagnesiation from D to E, peaks of $Mo^{3+}$ doublets emerge and $Mo^{2+}$ doublets decrease with 4-coordinated $S^{2-}$ unchanged, suggesting that $Mo^{2+}$ is oxidized


DOI: 10.1021/acsnano.9b08848
ACS Nano XXXX, XXX, XXX−XXX

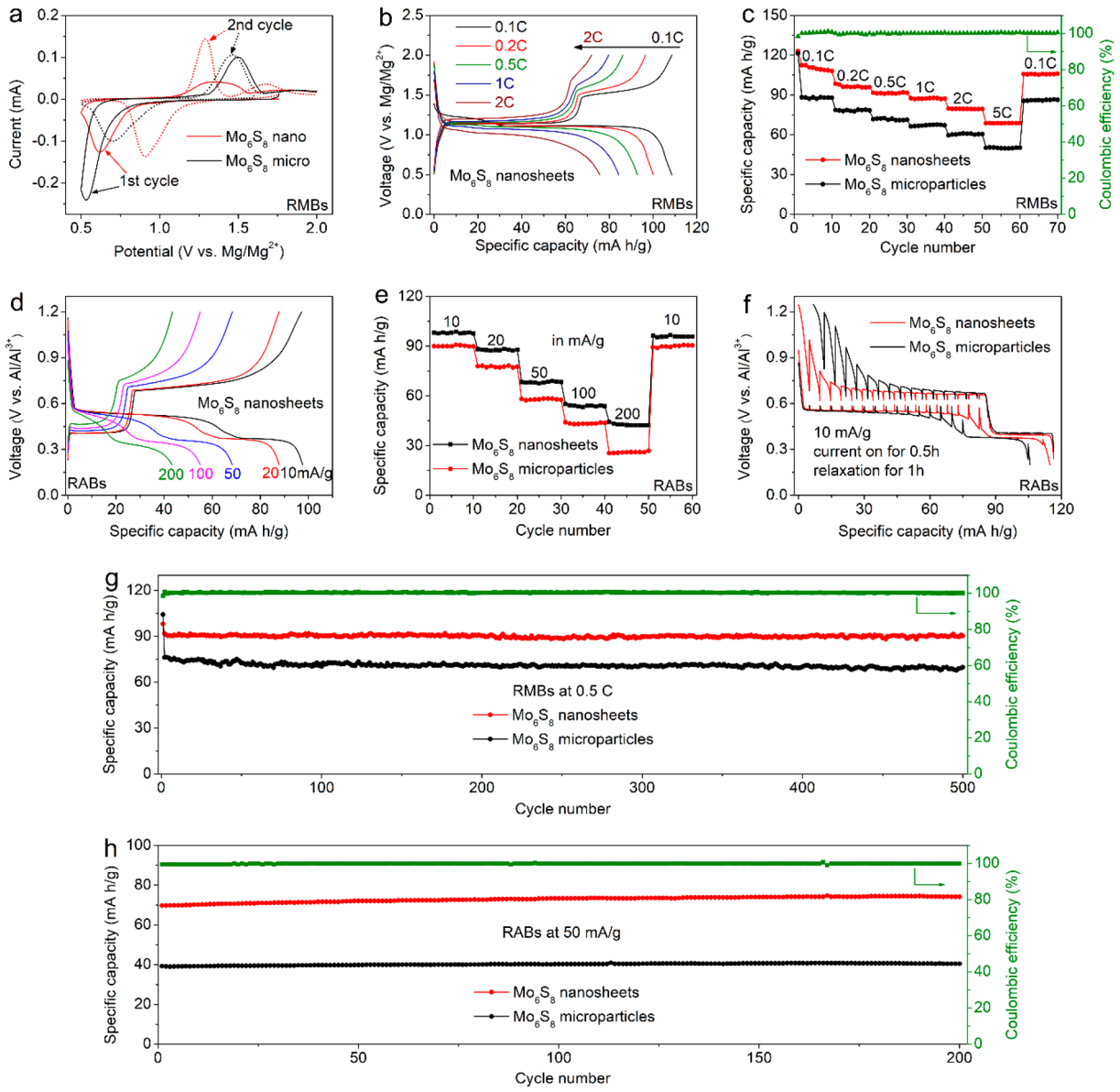


**Figure 3. Electrochemical performance of $Mo_6S_8$ nanosheets and microparticles in (a−c,g) APC/THF electrolyte between 0.5 and 2 V for RMBs and (d−f,h) $AlCl_3$-[BMIm]Cl ionic liquid electrolyte between 0.2 and 1.2 V for RABs at room temperature. (a) Cyclic voltammetry curves of $Mo_6S_8$ nanosheets and microparticles for the first two cycles at the scan rate of 0.05 mV/s in RMBs. (b) Current density dependence of discharge−charge curves of $Mo_6S_8$ nanosheets in RMBs. (c) Rate performance of $Mo_6S_8$ nanosheets and microparticles with current varying from 0.1 to 5C in RMBs. (d) Current density dependence of discharge−charge curves of $Mo_6S_8$ nanosheets in RABs. (e) Rate performance of $Mo_6S_8$ nanosheets and microparticles with current varying from 10 to 200 mA/g in RABs. (f) Quasi-equilibrium voltage profile of $Mo_6S_8$ nanosheets and microparticles obtained from galvanostatic intermittent titration technique in RABs. The cells were allowed to relax for 1 h after every 0.5 h discharging or charging at 10 mA/g in RABs. (g) Long-term cycling performance and Coulombic efficiency of $Mo_6S_8$ nanosheets and microparticles at 0.5C in RMBs. (h) Long-term cycling performance of $Mo_6S_8$ nanosheets and microparticles at 50 mA/g in RABs.**

to be $Mo^{3+}$ in the first charge plateau. Upon further demagnesiation to 2 V, two Mo 3d doublets do not evolve, whereas the 3-coordinated $S^{2-}$ doublet re-emerges, accompanied by 4-coordinated $S^{2-}$ doublet receding. Regarding the Mo 3d and S 2p core-level evolution upon galvanostatic discharge/charge, the magnesiation process occurs in two steps. In the first plateau, the charge transfer involves mainly sulfur atoms when the anion p-states arise to the top of the valence band and become dominant.[56,57] In the second plateau, the outer sites are filled, involving a reduction of $Mo^{3+}$ to $Mo^{2+}$, which shifts the Fermi level of $Mo_6S_8$ into its pseudogap, inducing metal to semiconductor transition.[58] Accordingly, the different $Mg^{2+}$ mobilities in $Mo_6S_8$ within the first and second plateau may originate from the polarization effects induced by sulfur anions. Once the Mg inner ring is formed, the activation energy of $Mg^{2+}$ seems to be lower, affording an increase in its mobility.[59]

## CONCLUSIONS

In this work, we proposed a facile approach to synthesize large-scale and high-purity $Mo_6S_8$ nanosheets by applying IVT. The reaction mechanism is carefully investigated by XRD, demonstrating the pivotal role of iodine. SEM, TEM, and


DOI: 10.1021/acsnano.9b08848
ACS Nano XXXX, XXX, XXX−XXX

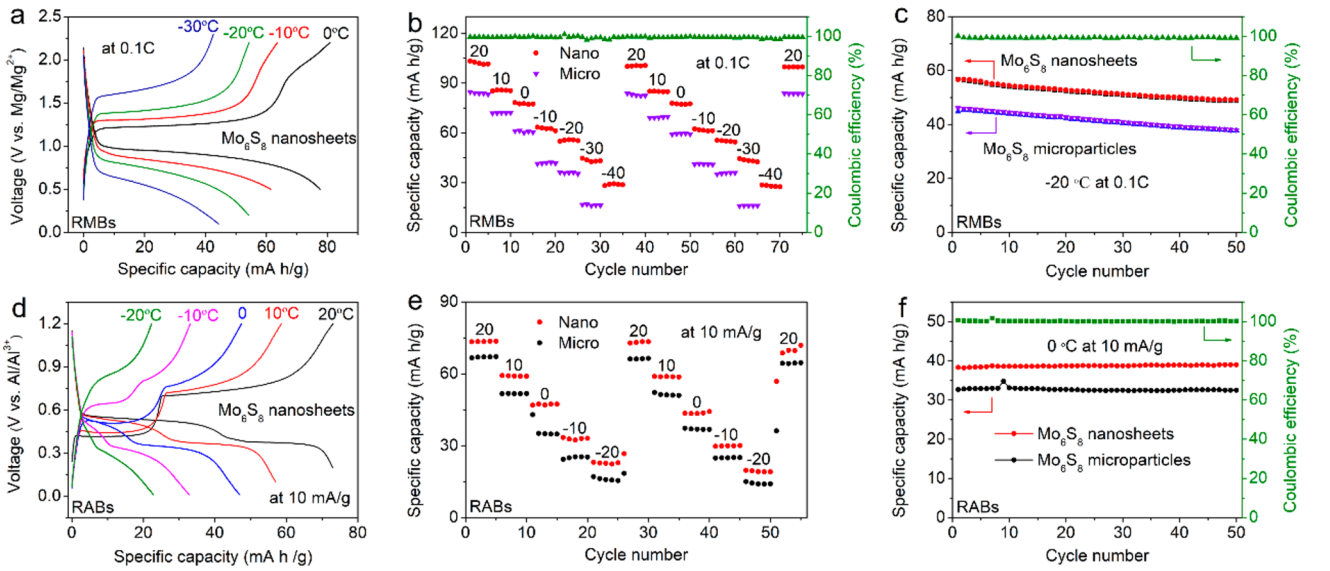


**Figure 4. Low-temperature performance of $Mo_6S_8$ nanosheets and microparticles in (a–c) APC/THF electrolyte between 0.5 and 2 V at 0.1C for RMBs and (d–f) $AlCl_3$-[BMIm]Cl ionic liquid electrolyte between 0.2 and 1.2 V at 10 mA/g for RABs. Typical discharge/charge curves of $Mo_6S_8$ nanosheets and microparticles at various temperatures in (a) RMBs and (d) RABs. Temperature dependence of capacities of $Mo_6S_8$ nanosheets and microparticles (b) from 20 to −40 °C in RMBs and (e) from 20 to −20 °C in RABs. Cycling performance of $Mo_6S_8$ nanosheets and microparticles (c) at 0.1C under −20 °C in RMBs and (d) at 10 mA/g under 0 in RABs.**

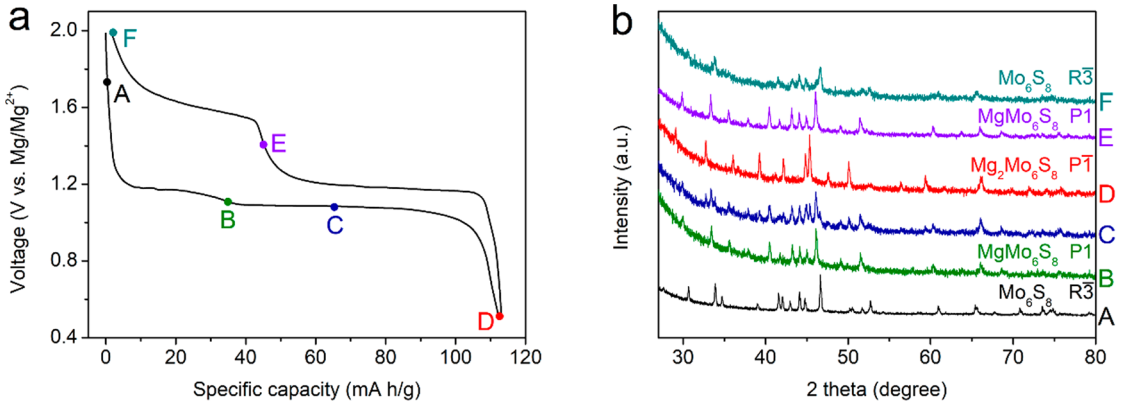


**Figure 5. Studies of the reaction mechanism of $Mo_6S_8$ nanosheets during discharge/charge. (a) Electrochemical discharge/charge profile labeling the points at which diffraction patterns are collected: (A) pristine $Mo_6S_8$, (B) discharged to 1.1 V, (C) on the second discharge plateau, (D) fully discharged to 0.5 V, (E) recharged to 1.4 V, (F) fully recharged to 2 V. (b) Corresponding *ex situ* XRD patterns of $Mo_6S_8$ nanosheets.**

STEM-LAADF were applied to characterize $Mo_6S_8$ nanosheets. When applied in rechargeable Mg and Al batteries, compared with $Mo_6S_8$ microparticles obtained *via* the conventional method, $Mo_6S_8$ nanosheets exhibit extraordinary electrochemical performances with faster kinetics especially at low temperatures. *Ex situ* XRD, EDS, and XPS demonstrate that $Mo_6S_8$ nanosheets undergo a phase-transition reaction upon magnesiation, and the charge transfer is initiated from sulfur anions followed by the valence change of molybdenum. In addition to the application in batteries, $Mo_6S_8$ nanosheets with ultrahigh surface area, high aspect ratio, and unusual surface chemistry would have wide applications including superconductivity, thermoelectricity, as well as catalysis. We also believe that IVT would offer a new way to synthesize a wide spectrum of inorganic compounds.

## EXPERIMENTAL SECTION

**Material Synthesis.** First, $MoS_2$, Cu, and Mo powders with the molar ratio of 2:1:1 were ball-milled for 2 h at 300 rpm under Ar. Then, the mixtures along with a small amount of iodine were pressed into pellets by a 14 mm diameter mold and sealed in a Swagelok stainless steel vessel, which was gradually heated to 800 °C at 2 °C/min and kept for 24 h under Ar. Subsequently, the as-prepared $Cu_2Mo_6S_8$ precursors were dispersed into a 6 M HCl solution for 12 h with oxygen bubbling to leach out Cu. After the reaction, the obtained $Mo_6S_8$ powder was centrifuged and washed with deionized water three times followed by drying at 60 °C overnight under vacuum.

**Material Characterizations.** The XRD patterns were measured using Cu K$\alpha$ radiation on an X'Pert Pro MPD X-ray diffractometer from 5 to 120° (2$\theta$). The morphologies of the samples were investigated by a SEM (Hitachi S-4800) with energy-disperse X-ray analysis. TEM images and selected area electron diffraction patterns were acquired using a FEI Tecnai F20 transmission electron microscope. The atomic force microscopy (AFM) images were obtained using a Bruker Dimension Icon AFM system. An AFM tip (SCANASYST-AIR, Bruker Nano Inc.) was applied to probe the


DOI: 10.1021/acsnano.9b08848
ACS Nano XXXX, XXX, XXX−XXX

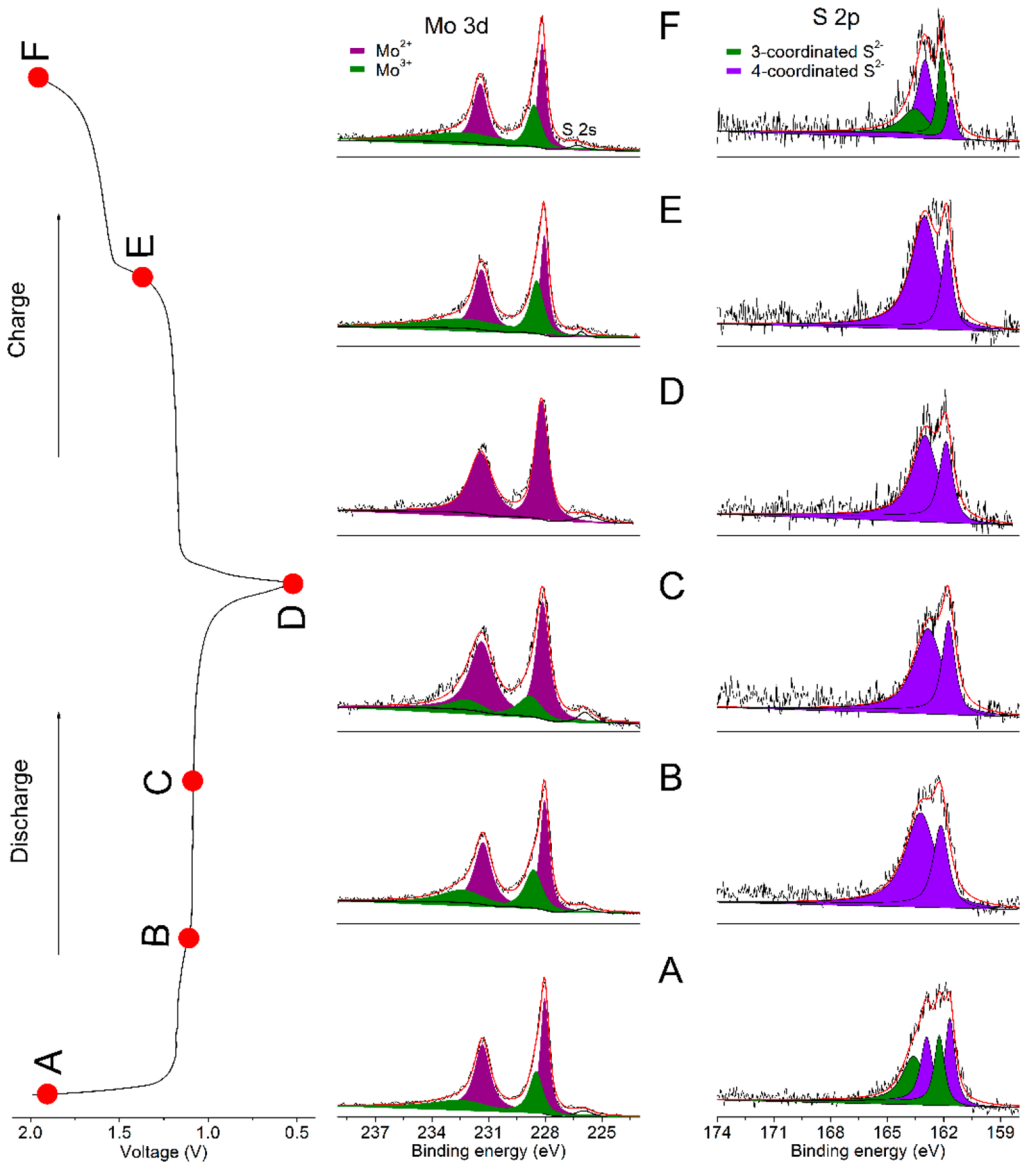


**Figure 6.** *Ex situ* XPS Mo 3d and S 2p peak evolution of the Chevrel phase $Mo_6S_8$ nanosheets registered at various stages: (A) pristine $Mo_6S_8$, (B) discharged to 1.1 V, (C) on the second discharge plateau, (D) fully discharged to 0.5 V, (E) recharged to 1.4 V, and (F) fully recharged to 2 V.

topography and thickness of the samples in the peak-force working mode. The Brunauer−Emmett−Teller measurements were carried out using a Micromeritics ASAP 2020 system. The X-ray photoelectron spectroscopy spectra were recorded with a spectrometer having Mg/Al K$\alpha$ radiation (ESCALAB 250 Xi, Thermo Fisher). All binding energies reported were corrected using the signal of the carbon at 284.8 eV as an internal standard. For the *ex situ* XPS measurements, the coin cells were disassembled in an argon-filled glovebox with different conditions, and the electrodes were washed in tetrahydrofuran three times to remove the electrolyte, then, the drying samples were obtained and moved to the machine with an argon-filled sealing tube as the transferred box. In this process, all samples were exposed to air within 3−4 s.

**Electrochemical Measurements.** Cell assembly was carried out in an Ar-filled glovebox with $O_2$ and $H_2O$ levels below 0.1 ppm. $Mo_6S_8$ electrodes were prepared by compressing the as-prepared powders, polytetrafluoroethylene, and ketjen black at a weight ratio of 8:1:1 onto the molybdenum grid. Electrochemical performance for rechargeable Mg batteries was tested in coin cells, with APC electrolyte, polished Mg metal as the anode, and Whatman glass fiber as separators. Rechargeable Al batteries were assembled using pouch cells, with $AlCl_3$-[BMIm]Cl ionic liquid electrolyte, polished Al metal as the anode, and Whatman glass fibers as separators. The electrochemistry was conducted on an Arbin battery test station (BT2000, Arbin Instruments, USA) with voltage cutoff of 0.5−2 V for RMBs and 0.2−1.2 V for RABs at room temperature. During GITT measurement, the electrode was discharged/charged at a pulse current of 10 mA/g for a duration of 1 or 0.5 h, followed by a relaxation of 1 h at open circuit to reach equilibrium potentials. Nyquist plots were recorded using Autolab PGSTAT302N (Metrohm, Switzerland) at a frequency range of 0.01−100 kHz.

## ASSOCIATED CONTENT

### Supporting Information

The Supporting Information is available free of charge at https://pubs.acs.org/doi/10.1021/acsnano.9b08848.

SEM of $Cu_2Mo_6S_8$ and $Mo_6S_8$, picture of $Mo_6S_8$ powder, BET, XRD Rietveld refinement fit, crystallographic and Rietveld refinement data of $Mo_6S_8$, electrochemical



DOI: 10.1021/acsnano.9b08848
ACS Nano XXXX, XXX, XXX−XXX

performance of $Mo_6S_8$, SEM images of cycled Mg and Al metal, EDS spectra of $Mo_6S_8$ nanosheets (PDF)

## AUTHOR INFORMATION


### Corresponding Author

*E-mail: suoliumin@iphy.ac.cn.

### ORCID

Lin Gu: 0000-0002-7504-031X
Liumin Suo: 0000-0002-6772-8421
Yong-Sheng Hu: 0000-0002-8430-6474
Hong Li: 0000-0002-8659-086X
Xuejie Huang: 0000-0001-5900-678X

### Author Contributions

‖M.M. and Z.L. contributed equally to this work.


### Notes

The authors declare no competing financial interest.

## ACKNOWLEDGMENTS

This work was supported by National Key Technologies R&D Program, China (2018YFB0104400), the National Natural Science Foundation of China (51872322, 21905299), the China Postdoctoral Science Foundation (2019TQ0346), and Shell Global Solutions International B.V. (Agreement No. PT76419).

## REFERENCES


(1) Chevrel, R.; Sergent, M.; Prigent, J. Sur De Nouvelles Phases Sulfurées Ternaires Du Molybdène. *J. Solid State Chem.* **1971**, *3*, 515−519.

(2) Sergent, M.; Chevrel, R. Sur De Nouvelles Phases Séléniées Ternaires Du Molybdène. *J. Solid State Chem.* **1973**, *6*, 433−437.

(3) Ling, C.; Suto, K. Thermodynamic Origin of Irreversible Magnesium Trapping in Chevrel Phase $Mo_6S_8$: Importance of Magnesium and Vacancy Ordering. *Chem. Mater.* **2017**, *29*, 3731−3739.

(4) Levi, E.; Lancry, E.; Mitelman, A.; Aurbach, D.; Ceder, G.; Morgan, D.; Isnard, O. Phase Diagram of Mg Insertion into Chevrel Phases, $Mg_xMo_6T_8$ (T = S, Se). 1. Crystal Structure of the Sulfides. *Chem. Mater.* **2006**, *18*, 5492−5503.

(5) Thöle, F.; Wan, L. F.; Prendergast, D. Re-Examining the Chevrel Phase $Mo_6S_8$ Cathode for Mg Intercalation from an Electronic Structure Perspective. *Phys. Chem. Chem. Phys.* **2015**, *17*, 22548−22551.

(6) Richard, J.; Benayad, A.; Colin, J. F.; Martinet, S. Charge Transfer Mechanism into the Chevrel Phase $Mo_6S_8$ During Mg Intercalation. *J. Phys. Chem. C* **2017**, *121*, 17096−17103.

(7) Matthias, B. T.; Marezio, M.; Corenzwit, E.; Cooper, A. S.; Barz, H. E. High-Temperature Superconductors, the First Ternary System. *Science* **1972**, *175*, 1465−1466.

(8) Yvon, K.; Paoli, A. Charge Transfer and Valence Electron Concentration in Chevrel Phases. *Solid State Commun.* **1977**, *24*, 41−45.

(9) Nunes, R. W.; Mazin, I. I.; Singh, D. J. Theoretical Search for Chevrel-Phase-Based Thermoelectric Materials. *Phys. Rev. B: Condens. Matter Mater. Phys.* **1999**, *59*, 7969−7972.

(10) Masschelein, P.; Candolfi, C.; Dauscher, A.; Gendarme, C.; Rabih, A. R. A. O.; Gougeon, P.; Potel, M.; Gall, P.; Gautier, R.; Lenoir, B. Influence of S and Te Substitutions on the Thermoelectric Properties of the Cluster Compound $Ag_{3.8}Mo_9Se_{11}$. *J. Alloys Compd.* **2018**, *739*, 360−367.

(11) Rabiller-Baudry, M.; Sergent, M.; Chevrel, R. Convenient Syntheses of Chevrel Phase Compounds from Soluble Sulfide Precursors under Flowing Hydrogen Atmosphere. *Mater. Res. Bull.* **1991**, *26*, 519−526.

(12) Kamiguchi, S.; Takeda, K.; Kajio, R.; Okumura, K.; Nagashima, S.; Chihara, T. Application of Solid-State Molybdenum Sulfide Clusters with an Octahedral Metal Framework to Catalysis: Ring-Opening of Tetrahydrofuran to Butyraldehyde. *J. Cluster Sci.* **2013**, *24*, 559−574.

(13) Aurbach, D.; Lu, Z.; Schechter, A.; Gofer, Y.; Gizbar, H.; Turgeman, R.; Cohen, Y.; Moshkovich, M.; Levi, E. Prototype Systems for Rechargeable Magnesium Batteries. *Nature* **2000**, *407*, 724−727.

(14) Tarascon, J. M.; Disalvo, F. J.; Murphy, D. W.; Hull, G. W.; Rietman, E. A.; Waszczak, J. V. Stoichiometry and Physical Properties of Ternary Molybdenum Chalcogenides $M_xMo_6X_8$ (X = S, Se; M = Li, Sn, Pb). *J. Solid State Chem.* **1984**, *54*, 204−212.

(15) Mulhern, P. J.; Haering, R. R. Rechargeable Nonaqueous Lithium/$Mo_6S_8$ Battery. *Can. J. Phys.* **1984**, *62*, 527−531.

(16) Uchida, T.; Watanabe, K.; Wakihara, M.; Taniguchi, M. Discharge Properties of $Mo_6S_{8.0}$ and $Cu_yMo_6S_{7.75}$ (y = 1.05 and 2.0) in Lithium Secondary Cells. *Chem. Lett.* **1985**, *14*, 1095−1098.

(17) Yue, J.; Zhu, X.; Han, F.; Fan, X.; Wang, L.; Yang, J.; Wang, C. Long Cycle Life All-Solid-State Sodium Ion Battery. *ACS Appl. Mater. Interfaces* **2018**, *10*, 39645−39650.

(18) Tarascon, J. M.; Hull, G. W.; Marsh, P.; Haar, T. Electrochemical, Structural, and Physical Properties of the Sodium Chevrel Phases $Na_xMo_6X_{8-y}I_y$ (X = S, Se and y = 0 to 2). *J. Solid State Chem.* **1987**, *66*, 204−224.

(19) Gocke, E.; Schramm, W.; Dolscheid, P.; Schöllhorn, R. Molybdenum Cluster Chalcogenides $Mo_6X_8$: Electrochemical Intercalation of Closed Shell Ions $Zn^{2+}$, $Cd^{2+}$, and Na. *J. Solid State Chem.* **1987**, *70*, 71−81.

(20) Fischer, C.; Gocke, E.; Stege, U.; Schöllhorn, R. Molybdenum Cluster Chalcogenides: *In Situ* X-Ray Studies on the Formation of $Cu_xMo_6S_8$ *Via* Electron/Ion Transfer. *J. Solid State Chem.* **1993**, *102*, 54−68.

(21) Saha, P.; Jampani, P. H.; Datta, M. K.; Okoli, C. U.; Manivannan, A.; Kumta, P. N. A Convenient Approach to $Mo_6S_8$ Chevrel Phase Cathode for Rechargeable Magnesium Battery. *J. Electrochem. Soc.* **2014**, *161*, A593−A598.

(22) Wan, L. F.; Perdue, B. R.; Apblett, C. A.; Prendergast, D. Mg Desolvation and Intercalation Mechanism at the $Mo_6S_8$ Chevrel Phase Surface. *Chem. Mater.* **2015**, *27*, 5932−5940.

(23) Cheng, Y.; Luo, L.; Zhong, L.; Chen, J.; Li, B.; Wang, W.; Mao, S. X.; Wang, C.; Sprenkle, V. L.; Li, G.; Liu, J. Highly Reversible Zinc-Ion Intercalation into Chevrel Phase $Mo_6S_8$ Nanocubes and Applications for Advanced Zinc-Ion Batteries. *ACS Appl. Mater. Interfaces* **2016**, *8*, 13673−13677.

(24) Schöllhorn, R.; Kümpers, M.; Besenhard, J. O. Topotactic Redox Reactions of the Channel Type Chalcogenides $Mo_3S_4$ and $Mo_3Se_4$. *Mater. Res. Bull.* **1977**, *12*, 781−788.

(25) Geng, L.; Lv, G.; Xing, X.; Guo, J. Reversible Electrochemical Intercalation of Aluminum in $Mo_6S_8$. *Chem. Mater.* **2015**, *27*, 4926−4929.

(26) Mao, M.; Ji, X.; Hou, S.; Gao, T.; Wang, F.; Chen, L.; Fan, X.; Chen, J.; Ma, J.; Wang, C. Tuning Anionic Chemistry to Improve Kinetics of Mg Intercalation. *Chem. Mater.* **2019**, *31*, 3183−3191.

(27) Cheng, Y.; Parent, L. R.; Shao, Y.; Wang, C.; Sprenkle, V. L.; Li, G.; Liu, J. Facile Synthesis of Chevrel Phase Nanocubes and Their Applications for Multivalent Energy Storage. *Chem. Mater.* **2014**, *26*, 4904−4907.

(28) Fischer, Ø. Chevrel Phases: Superconducting and Normal State Properties. *Appl. Phys.* **1978**, *16*, 1−28.

(29) Chevrel, R.; Sergent, M.; Prigent, J. Un Nouveau Sulfure De Molybdene: $Mo_3S_4$ Preparation, Proprietes Et Structure Cristalline. *Mater. Res. Bull.* **1974**, *9*, 1487−1498.

(30) Kondo, S.; Takada, K.; Yamamura, Y.; Gyoten, H.; Yoshida, S. A New Synthetic Method for Chevrel-Phase Compounds. *Solid State Ionics* **1992**, *57*, 147−151.

(31) Yamamoto, S.; Matsui, K.; Wakihara, M.; Taniguchi, M. Stable Range of Copper Molybdenum Sulfide $Cu_xMo_6S_{8-y}$ and Measure-




DOI: 10.1021/acsnano.9b08848
ACS Nano XXXX, XXX, XXX−XXX

ment of the Superconducting Critical Temperature Tc. *Mater. Res. Bull.* **1983**, *18*, 1311−1316.
(32) Tarascon, J. M.; Waszczak, J. V.; Hull, G. W.; DiSalvo, F. J.; Blitzer, L. D. Synthesis and Physical Properties of New Superconducting Chevrel Phases $Hg_xMo_6S_8$. *Solid State Commun.* **1983**, *47*, 973−979.
(33) Cheung, K. Y.; Steele, B. C. H. Homogeneity Range of Copper Molybdenum Sulphide $Cu_xMo_6S_{8-y}$. *Mater. Res. Bull.* **1980**, *15*, 1717−1725.
(34) Flukiger, R.; Devantay, H.; Jorda, J.; Muller, J. Metallurgical and Physical Properties of Ternary Molybdenum Sulfides ($M_xMo_3S_4$) as Synthetized in the Bulk State. *IEEE Trans. Magn.* **1977**, *13*, 818−820.
(35) Wakihara, M.; Hinode, H.; Inoue, C. Decomposition of No Using Chevrel-Phase Sulfides. *Solid State Ionics* **1992**, *53*−*56*, 413−417.
(36) Aurbach, D.; Suresh, G. S.; Levi, E.; Mitelman, A.; Mizrahi, O.; Chusid, O.; Brunelli, M. Progress in Rechargeable Magnesium Battery Technology. *Adv. Mater.* **2007**, *19*, 4260−4267.
(37) Lancry, E.; Levi, E.; Mitelman, A.; Malovany, S.; Aurbach, D. Molten Salt Synthesis (MSS) of $Cu_2Mo_6S_8$—New Way for Large-Scale Production of Chevrel Phases. *J. Solid State Chem.* **2006**, *179*, 1879−1882.
(38) Gershinsky, G.; Haik, O.; Salitra, G.; Grinblat, J.; Levi, E.; Daniel Nessim, G.; Zinigrad, E.; Aurbach, D. Ultra Fast Elemental Synthesis of High Yield Copper Chevrel Phase with High Electrochemical Performance. *J. Solid State Chem.* **2012**, *188*, 50−58.
(39) Saha, P.; Jampani, P. H.; Datta, M. K.; Hong, D.; Gattu, B.; Patel, P.; Kadakia, K. S.; Manivannan, A.; Kumta, P. N. A Rapid Solid-State Synthesis of Electrochemically Active Chevrel Phases ($Mo_6T_8$; T= S, Se) for Rechargeable Magnesium Batteries. *Nano Res.* **2017**, *10*, 4415−4435.
(40) Binnewies, M.; Glaum, R.; Schmidt, M.; Schmidt, P. Chemical Vapor Transport Reactions − A Historical Review. *Z. Anorg. Allg. Chem.* **2013**, *639*, 219−229.
(41) Li, S.; Wang, S.; Tang, D.-M.; Zhao, W.; Xu, H.; Chu, L.; Bando, Y.; Golberg, D.; Eda, G. Halide-Assisted Atmospheric Pressure Growth of Large $WSe_2$ and $WS_2$ Monolayer Crystals. *Appl. Mater. Today* **2015**, *1*, 60−66.
(42) Zhou, J.; Lin, J.; Huang, X.; Zhou, Y.; Chen, Y.; Xia, J.; Wang, H.; Xie, Y.; Yu, H.; Lei, J.; Wu, D.; Liu, F.; Fu, Q.; Zeng, Q.; Hsu, C.-H.; Yang, C.; Lu, L.; Yu, T.; Shen, Z.; Lin, H.; et al. A Library of Atomically Thin Metal Chalcogenides. *Nature* **2018**, *556*, 355−359.
(43) Chen, X.; Bleken, F. L.; Løvvik, O. M.; Vullum-Bruer, F. Comparing Electrochemical Performance of Transition Metal Silicate Cathodes and Chevrel Phase $Mo_6S_8$ in the Analogous Rechargeable Mg-Ion Battery System. *J. Power Sources* **2016**, *321*, 76−86.
(44) Lancry, E.; Levi, E.; Gofer, Y.; Levi, M.; Salitra, G.; Aurbach, D. Leaching Chemistry and the Performance of the $Mo_6S_8$ Cathodes in Rechargeable Mg Batteries. *Chem. Mater.* **2004**, *16*, 2832−2838.
(45) Xue, W.; Shi, Z.; Suo, L.; Wang, C.; Wang, Z.; Wang, H.; So, K. P.; Maurano, A.; Yu, D.; Chen, Y.; Qie, L.; Zhu, Z.; Xu, G.; Kong, J.; Li, J. Intercalation-Conversion Hybrid Cathodes Enabling Li−S Full-Cell Architectures with Jointly Superior Gravimetric and Volumetric Energy Densities. *Nature Energy* **2019**, *4*, 374−382.
(46) Momma, K.; Izumi, F. Vesta 3 for Three-Dimensional Visualization of Crystal, Volumetric and Morphology Data. *J. Appl. Crystallogr.* **2011**, *44*, 1272−1276.
(47) Suo, L.; Borodin, O.; Gao, T.; Olguin, M.; Ho, J.; Fan, X.; Luo, C.; Wang, C.; Xu, K. Water-in-Salt" Electrolyte Enables High-Voltage Aqueous Lithium-Ion Chemistries. *Science* **2015**, *350*, 938−943.
(48) Geng, L.; Scheifers, J. P.; Zhang, J.; Bozhilov, K. N.; Fokwa, B. P. T.; Guo, J. Crystal Structure Transformation in Chevrel Phase $Mo_6S_8$ Induced by Aluminum Intercalation. *Chem. Mater.* **2018**, *30*, 8420−8425.
(49) Mei, L.; Xu, J.; Wei, Z.; Liu, H.; Li, Y.; Ma, J.; Dou, S. Chevrel Phase $Mo_6T_8$ (T = S, Se) as Electrodes for Advanced Energy Storage. *Small* **2017**, *13*, 1701441.
(50) Suresh, G. S.; Levi, M. D.; Aurbach, D. Effect of Chalcogen Substitution in Mixed $Mo_6S_{8-n}Se_n$ (n = 0, 1, 2) Chevrel Phases on the Thermodynamics and Kinetics of Reversible Mg Ions Insertion. *Electrochim. Acta* **2008**, *53*, 3889−3896.
(51) Ritter, C.; Gocke, E.; Fischer, C.; Schöllhorn, R. Neutron Diffraction Study on the Crystal Structure of Lithium Intercalated Chevrel Phases. *Mater. Res. Bull.* **1992**, *27*, 1217−1225.
(52) Mao, M.; Gao, T.; Hou, S.; Wang, F.; Chen, J.; Wei, Z.; Fan, X.; Ji, X.; Ma, J.; Wang, C. High-Energy-Density Rechargeable Mg Battery Enabled by a Displacement Reaction. *Nano Lett.* **2019**, *19*, 6665−6672.
(53) Mao, M.; Gao, T.; Hou, S.; Wang, C. A Critical Review of Cathodes for Rechargeable Mg Batteries. *Chem. Soc. Rev.* **2018**, *47*, 8804−8841.
(54) Yoo, H. D.; Shterenberg, I.; Gofer, Y.; Gershinsky, G.; Pour, N.; Aurbach, D. Mg Rechargeable Batteries: An On-Going Challenge. *Energy Environ. Sci.* **2013**, *6*, 2265−2279.
(55) Levi, E.; Lancry, E.; Mitelman, A.; Aurbach, D.; Isnard, O.; Djurado, D. Phase Diagram of Mg Insertion into Chevrel Phases, $Mg_xMo_6T_8$ (T = S, Se). 2. The Crystal Structure of Triclinic $MgMo_6Se_8$. *Chem. Mater.* **2006**, *18*, 3705−3714.
(56) Umrigar, C.; Ellis, D. E.; Wang, D.-S.; Krakauer, H.; Posternak, M. Band Structure, Intercalation, and Interlayer Interactions of Transition-Metal Dichalcogenides: $TiS_2$ and $LiTiS_2$. *Phys. Rev. B: Condens. Matter Mater. Phys.* **1982**, *26*, 4935−4950.
(57) Kim, Y.-S.; Kim, H.-J.; Jeon, Y.-A.; Kang, Y.-M. Theoretical Study on the Correlation between the Nature of Atomic Li Intercalation and Electrochemical Reactivity in $TiS_2$ and $TiO_2$. *J. Phys. Chem. A* **2009**, *113*, 1129−1133.
(58) Wan, L. F.; Wright, J.; Perdue, B. R.; Fister, T. T.; Kim, S.; Apblett, C. A.; Prendergast, D. Revealing Electronic Structure Changes in Chevrel Phase Cathodes Upon Mg Insertion Using X-Ray Absorption Spectroscopy. *Phys. Chem. Chem. Phys.* **2016**, *18*, 17326−17329.
(59) Levi, M. D.; Lancry, E.; Gizbar, H.; Gofer, Y.; Levi, E.; Aurbach, D. Phase Transitions and Diffusion Kinetics During $Mg^{2+}$- and $Li^+$-Ion Insertions into the $Mo_6S_8$ Chevrel Phase Compound Studied by PITT. *Electrochim. Acta* **2004**, *49*, 3201−3209.


DOI: 10.1021/acsnano.9b08848
*ACS Nano* XXXX, XXX, XXX−XXX